PHYSICAL REVIEW B **100**, 085410 (2019)

Nonlocal transport in superconducting heterostructures based on Weyl semimetals

Hai Li[*] and Gang Ouyang[†]
Key Laboratory of Low-Dimensional Quantum Structures and Quantum Control of Ministry of Education, Synergetic Innovation Center for Quantum Effects and Applications (SICQEA), Hunan Normal University, Changsha 410081, China

(Received 5 June 2019; revised manuscript received 15 July 2019; published 8 August 2019)

We investigate the nonlocal transport properties in normal/superconducting/normal (NSN) junctions based on time-reversal symmetric type-I and type-II Weyl semimetals (WSMs). In the type-I WSM-based NSN junction, we show that a crossed-Andreev-reflection-dominated nonlocal transport can be realized within wide ranges of related parameters, which is favorable for the Cooper-pair splitting. For the type-II WSM-based NSN junction, we focus on the manifestations of the anisotropic aspects of type-II WSMs in the nonlocal transport. Owing to the hyperboloidlike Fermi surfaces of type-II WSMs, the scattering configurations and nonlocal differential conductance are strongly anisotropic, differing from the scenarios in similar NSN junctions based on other Dirac materials. These results enrich the understanding of the correlated transport in time-reversal symmetric WSM-based superconducting heterostructures.

DOI: 10.1103/PhysRevB.100.085410

I. INTRODUCTION

Weyl semimetals (WSMs) are paradigms of gapless topological phases of matter in three dimensions, possessing linear band crossings at isolated Weyl nodes in momentum space [1–4]. The emergence of nontrivial and robust Weyl nodes requires the breaking of either time-reversal [2,5] or inversion symmetry [6,7], and the Weyl nodes always arise in pairs of opposite chirality [8]. In principle, the WSMs can be classified into two subgroups, i.e., type-I and type-II WSMs, and which cannot be smoothly deformed into each other [1,3]. The type-I WSMs have been materialized in the transition metal monopnictides [9–13], which possess closed constant energy surfaces. Whereas, the type-II WSMs host overtilted Weyl cones [1,3] and open constant energy surfaces. The materialization of type-II WSMs has been achieved in several systems, including $\mathrm{MoTe_2}$ [14–16], $\mathrm{TaIrTe_4}$ [17], and LaAlGe [18]. These achievements hold promise for further engineering and detecting novel states in various hybrid structures based on WSMs [19–32], such as the superconducting correlations in WSM-based superconducting heterostructures (SHSs) [20–32].

Resorting to the proximity effect, it is possible to realize superconducting correlations by combining WSMs with ordinary superconductors, as has been experimentally proposed in SHSs based on both type-I [20] and type-II WSMs [21]. In a SHS with idea contacts, the subgap transport is dominated by a phase coherent scattering process known as Andreev reflection [33–35]. In a time-reversal symmetric type-I WSM/*s*-wave superconductor heterostructure, it has been revealed that a universal zero-bias differential conductance per channel can be obtained, owing to the interaction between the spin/orbital-momentum locking and *s*-wave pairing in the proposed setup [26]. While the stories are quite different in a type-II WSM-based SHS, it has been proposed that there exist double Andreev reflections, due to the overtilted Weyl cones of type-II WSMs [27]. Moreover, the band structure tilting also manifests itself in the nonlocal transport in a type-II WSMs-based multi-interface SHS deposited along the largest tilting direction. As reported in Ref. [28], both the double crossed Andreev reflection (CAR) and double elastic cotunneling (EC) processes emerge, in contrast to the scattering configurations in similar SHSs based on conventional [33,35] and other Dirac materials [36–43].

Based on the remarkable low-lying physics of WSMs [1,3] as well as the significant achievements in the fabrication of WSM-based SHSs [20,21], we propose two normal/superconducting/normal (NSN) junctions, respectively, based on the time-reversal symmetric type-I and type-II WSMs. The motivation of this work comes from the following two facts. On the one hand, we note that most experimentally well demonstrated type-I WSMs are time-reversal symmetric [9–13], and to the best of our knowledge, the nonlocal transport properties in NSN junctions based on this type of WSMs have not been concerned up to now. On the other hand, since the type-II WSM possesses overtilted Weyl cones, it has been theoretically demonstrated that the type-II-WSM-based NSN junction harbors double CAR and EC processes when the junction is arranged along the largest tilting direction of Weyl cones. However, the manifestations of the anisotropic band structures in the nonlocal transport properties have not been completely investigated. Following this line, we devote this work to exploring the nonlocal transport properties in time-reversal symmetric type-I and type-II WSMs-based NSN junctions. In the proposed type-I WSM-based NSN junction, it is revealed that the CAR transport probability vanishes for normal incidence, in contrast to those in similar NSN junctions based on graphene [36,42] and silicene [40,43]. Intriguingly, a CAR-dominated nonlocal transport can be achieved within wide ranges of relevant parameters, which

---

[*] hnnuhl@hunnu.edu.cn
[†] gangouy@hunnu.edu.cn

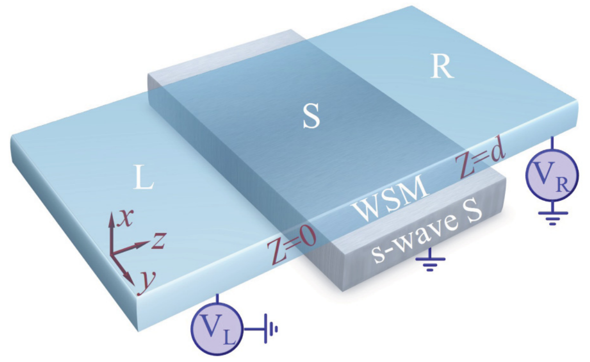

FIG. 1. Schematic of a type-I WSM-based NSN junction, where the superconducting electrode in the S region ($0 < z < d$) is grounded and the two normal regions denoted by L ($z < 0$) and R ($z > d$) are locally gated by V_L and V_R, respectively. The junction is assumed to extend to infinity in the xy plane.

is favorable for realizing the Cooper-pair splitting. Regarding the type-II WSM-based NSN junction, we mainly concentrate on the manifestations of the anisotropic aspects of type-II WSMs in the nonlocal transport. It is found that the scattering configurations and nonlocal differential conductance are strongly dependent on the interface orientation angle, apparently differing from those in similar NSN junctions based on other Dirac materials [36,38,40–43].

The remainder of this paper is organized as follows. The transport properties of the type-I WSM-based NSN junction are presented in Sec. II. In Sec. III, we focus on the nonlocal transport properties in a type-II WSM-based NSN junction. Finally, the conclusion is briefly drawn in Sec. IV.

II. NSN JUNCTIONS BASED ON TYPE-I WSMs

The proposed type-I WSM-based NSN junction is schematically shown in Fig. 1, where two local gate electrodes V_L and V_R are, respectively, deposited in the L ($z < 0$) and R ($z > d$) regions to independently tune the carrier densities therein. The superconductivity in the middle region ($0 < z < d$) is induced by an s-wave superconductor via the proximity effect. In practice, a recent experiment suggests the proposed setup could be realized in the system of NbAs by ion milling [20], based on the fact that Nb is an intrinsic superconductor and NbAs is a well-characterized type-I WSM preserving time-reversal symmetry [13]. We assume that in the proposed setup the translational symmetry is preserved in the xy plane, so that the transverse momenta $k_\parallel \equiv (k_x, k_y)$ can be treated as good quantum numbers [34–36,44]. Moreover, under this assumption the boundary effects can be safely neglected and the transport properties are dominated by the bulk states. In the framework of a Bogoliubov–de Gennes (BdG) equation [26,27,44], the nonlocal transport properties along the z direction are investigated by virtue of the scattering matrix method.

A. Model and formalism

According to the Fermi-doubling theorem [8], a time-reversal symmetric WSM contains at least four Weyl nodes. For simplicity, we take a time-reversal symmetric type-I WSM with four Weyl nodes as the prototype. It has been demonstrated that the s-wave superconducting paring couples a pair of electrons with the same chirality. Moreover, as has been proposed in Ref. [26], the interorbital pairing is strongly suppressed and only the intraorbital pairing is important. If the Weyl nodes are well separated in momentum space, the effective BdG Hamiltonian can be divided into two independent subsystems with opposite chiralities. Under these lines, it suffices to only consider the subsystem with positive chirality, and the corresponding BdG Hamiltonian takes the form of [26]

$$\mathcal{H}_{\mathrm{I}} = \begin{pmatrix} \hat{h}^{\mathrm{I}}_{+}(k) - \mu(z) & \hat{\Delta}(z) \\ \hat{\Delta}^{\dagger}(z) & -h^{\mathrm{I}}_{+}(k) + \mu(z) \end{pmatrix}, \tag{1}$$

which acts on the basis of $\psi = (\psi_{Q_+,\uparrow}, \psi_{Q_+,\downarrow}, \psi^*_{-Q_+,\downarrow}, -\psi^*_{-Q_+,\uparrow})^T$, where $\pm Q_+$ denotes a pair of time-reversed Weyl nodes with positive chiralities and T indicates the transpose operation. The single-particle effective Hamiltonian $\hat{h}^{\mathrm{I}}_{+}(k) = \hbar v(k_x\hat{\sigma}_1 + k_y\hat{\sigma}_2 - i\partial_z\hat{\sigma}_3)$ depicts the low-lying physics near the Weyl node, with $\hat{\sigma}_{1,2,3}$ the three Pauli matrices and v the Fermi velocity. The parameter $\mu(z) = \mu_L\Theta(-z) + \mu_S\Theta(z)\Theta(d-z) + \mu_R\Theta(z-d)$, where $\Theta(\cdot)$ symbolizes the Heaviside step function. We assume that the Fermi wavelength of the superconducting (S) region is much smaller than those of normal (N) regions, so that the leakage of Cooper pairs can be safely neglected [43,44]. In doing so, the pair potential can be rationally described by a step function model, viz., $\hat{\Delta}(z) = \Delta_0\hat{\sigma}_0 e^{i\varphi}\Theta(z)\Theta(d-z)$, with φ the superconducting phase. By diagonalizing the Hamiltonian shown in Eq. (1), the energy dispersion in the S region can be formulated as

$$\varepsilon_\lambda = \lambda\sqrt{\left(\hbar v\sqrt{k_z^2 + |k_\parallel|^2} \pm \mu_S\right)^2 + \Delta_0^2}, \tag{2}$$

with $\lambda = \pm 1$. For a set of fixed energy ε and transverse momentum $k_\parallel$, Eq. (2) gives four different roots of k_z, implying that there are four basis scattering states ψ^S_ν ($\nu = 1, 2, 3, 4$), thus the wave function in the S region should be

$$\Psi_S = \sum_{\nu=1}^{4} s_\nu \psi^S_\nu, \tag{3}$$

where the corresponding scattering amplitudes are parametrized by s_ν and the details of ψ^S_ν are shown in Eq. (A1).

In the two N regions, the dispersion relations can be written as

$$\varepsilon^{e(h)}_j = \pm\hbar v\sqrt{\left(k^{e(h)}_{j,z}\right)^2 + |k_\parallel|^2} - (+)\mu_j, \tag{4}$$

where $j = L, R$, respectively, indicate the related quantities of the left (L) and right (R) N regions, and the superscripts e and h denote the electronlike and holelike excitation spectra, respectively. Resorting to the dispersion relations we have

$$k^{e(h)}_{j,z} = \mathrm{sgn}[\epsilon + (-)\mu_j + |k_\parallel|]\sqrt{[\varepsilon + (-)\mu_j]^2/(\hbar v)^2 - |k_\parallel|^2}. \tag{5}$$

Accordingly, $|\varepsilon + (-)\mu_j| - |k_\parallel| \geqslant 0$ should be satisfied to get propagating electronlike (holelike) modes. Whereas, for the case of $|\varepsilon + (-)\mu_j| - |k_\parallel| < 0$, the corresponding modes are evanescent ones which do not contribute to the transport. In the L region, an electronlike incident quasiparticle can either be normally reflected as an electronlike one or be locally Andreev reflected as a holelike one, thus the related wave function is given by

$$\Psi_L = \psi^e_{L,+} + r^{ee}\psi^e_{L,-} + r^{he}\psi^h_{L,-}, \tag{6}$$

with r^{ee} and r^{he} the scattering amplitudes for the normal reflection (NR) and the local Andreev reflection (LAR), respectively. The basis scattering states $\psi^{e,h}_{j,\pm}$ can be obtained by solving the BdG equation $\mathcal{H}_{\mathrm{I}}\psi = \varepsilon\psi$ straightforwardly, and the details are given by Eq. (A3). On the other hand, the incident electronlike quasiparticle can tunnel into the R region as a holelike one through the CAR process or as an electronlike one via the EC process. Consequently, the wave function of the R region is given by

$$\Psi_R = t^{he}\psi^h_{R,+} + t^{ee}\psi^e_{R,+}, \tag{7}$$

where $t^{he(ee)}$ parametrizes the transmission amplitude for the CAR (EC) process.

To model the effects resulting from the interfacial defects and lattice mismatch, we introduce two interfacial barriers U_L and U_R arranged within the regions of $-d_L/2 < z < d_L/2$ and $d - d_R/2 < z < d + d_R/2$, respectively. In this work, we take the limits of $U_{L(R)} \to \infty$ and $d_{L(R)} \to 0$ with $U_{L(R)}d_{L(R)}/(\hbar v) \equiv Z_{L(R)}$ being finite. In the barrier regions, by substituting μ_j with U_j $(j = L, R)$ into Eq. (5), the expressions of the z components of momenta $k^{e,h}_{B,j,z}$ can be obtained, and the basis scattering states $\psi^{e,h}_{B,j,\pm}$ are shown in Eq. (A3) by substituting $k^{e,h}_{j,z}$ with $k^{e,h}_{B,j,z}$. In doing so, the related wave functions can be expressed as

$$\Psi_{BL} = b_1\psi^e_{B,L,+} + b_2\psi^e_{B,L,-} + b_3\psi^h_{B,L,+} + b_4\psi^h_{B,L,-}, \tag{8a}$$

$$\Psi_{BR} = c_1\psi^e_{B,R,+} + c_2\psi^e_{B,R,-} + c_3\psi^h_{B,R,+} + c_4\psi^h_{B,R,-}, \tag{8b}$$

where b_ν and c_ν label the related scattering amplitudes.

The scattering amplitudes can be determined by matching corresponding wave functions at the boundaries, to wit, $\Psi_L|_{z=-d_L/2} = \Psi_{BL}|_{z=-d_L/2}$, $\Psi_{BL}|_{z=0} = \Psi_S|_{z=0}$, $\Psi_S|_{z=d} = \Psi_{BR}|_{z=d}$, and $\Psi_{BR}|_{z=(d+d_R/2)} = \Psi_R|_{z=(d+d_R/2)}$, which automatically ensure the current conservation in the z direction. Consequently, the probabilities for the NR and LAR processes can be defined as

$$R^{ee} = \left|\frac{\langle\psi^e_{L,-}|\mathcal{J}^{\mathrm{I}}_z|\psi^e_{L,-}\rangle}{\langle\psi^e_{L,+}|\mathcal{J}^{\mathrm{I}}_z|\psi^e_{L,+}\rangle}\right||r^{ee}|^2, \tag{9a}$$

$$R^{he} = \left|\frac{\langle\psi^h_{L,-}|\mathcal{J}^{\mathrm{I}}_z|\psi^h_{L,-}\rangle}{\langle\psi^e_{L,+}|\mathcal{J}^{\mathrm{I}}_z|\psi^e_{L,+}\rangle}\right||r^{he}|^2. \tag{9b}$$

The particle current density operator $\mathcal{J}^{\mathrm{I}}_z \equiv \frac{-i}{\hbar}[z, \mathcal{H}_{\mathrm{I}}] = v\tau_3 \otimes \sigma_3$, with τ_3 the Pauli matrix operating on the Nambu space. For the EC and CAR processes, the related scattering probabilities are

$$T^{ee} = \left|\frac{\langle\psi^e_{R,+}|\mathcal{J}^{\mathrm{I}}_z|\psi^e_{R,+}\rangle}{\langle\psi^e_{L,+}|\mathcal{J}^{\mathrm{I}}_z|\psi^e_{L,+}\rangle}\right||t^{ee}|^2, \tag{10a}$$

$$T^{he} = \left|\frac{\langle\psi^h_{R,+}|\mathcal{J}^{\mathrm{I}}_z|\psi^h_{R,+}\rangle}{\langle\psi^e_{L,+}|\mathcal{J}^{\mathrm{I}}_z|\psi^e_{L,+}\rangle}\right||t^{he}|^2. \tag{10b}$$

Resorting to the scattering probabilities, the zero-temperature differential conductances for the CAR and EC processes can, respectively, be formulated as

$$\frac{\partial I^{\mathrm{I}}_{\mathrm{CAR}}}{\partial V} = \frac{4e^2A}{h}\int\frac{d\boldsymbol{k}_\parallel}{(2\pi)^2}T^{he}(eV, k_\parallel), \tag{11a}$$

$$\frac{\partial I^{\mathrm{I}}_{\mathrm{EC}}}{\partial V} = \frac{4e^2A}{h}\int\frac{d\boldsymbol{k}_\parallel}{(2\pi)^2}T^{ee}(eV, k_\parallel), \tag{11b}$$

with A the cross-sectional area of the junction and V the bias voltage. Consequently, the nonlocal differential conductance can be defined as $\partial I^{\mathrm{I}}_{nl}/\partial V = \partial I^{\mathrm{I}}_{\mathrm{EC}}/\partial V - \partial I^{\mathrm{I}}_{\mathrm{CAR}}/\partial V$. In addition, by virtue of the Blonder-Tinkham-Klapwijk (BTK) formula [34], the zero-temperature differential conductance for the local transport can be written as

$$\frac{\partial I^{\mathrm{I}}_l}{\partial V} = \frac{e^2A}{h}\int\frac{dk_\parallel}{(2\pi)^2}[1 - R^{ee}(eV, k_\parallel) + R^{he}(eV, k_\parallel)]. \tag{12}$$

To normalize the differential conductance, it is convenient to define $g^{\mathrm{I}}_0(eV) = e^2A(eV + \mu_L)^2/(\pi h)$, which is the conductance for a corresponding normal junction in the ballistic limit, or alternatively, $g^{\mathrm{I}}_0(eV)$ can also be viewed as the number of available channels at energy $(\mu_L + eV)$.

B. Results and discussion

In this section, we present the numerical results and uncover the underlying mechanisms for realizing the exclusive CAR transport in the type-I WSM-based NSN junction. In the numerical calculations, the chemical potential in the S region is fixed as $\mu_S = 50\Delta_0$ for definiteness.

The scattering probabilities for the normal incidence, i.e., the incident angle $\alpha = 0$, are shown in Figs. 2(a) and 2(b). As can be seen, the most prominent feature is the vanishing of the CAR process, i.e., $T^{he} = 0$, due to the spin/orbital momentum locking together with the s-wave pairing. This phenomenon is distinctly different from the scenarios in similar NSN junctions based on graphene [36,42] and silicene [40,43]. The spin/orbital-momentum texture also manifests itself in the disappearance of the backscattering for $\alpha = 0$, i.e., $R^{ee} = 0$, differing from that in conventional-material-based NSN junction [45,46].

We now focus on the CAR process which can split a Cooper pair into two entangled electrons separated spatially. Generally, in a type-I WSM-based NSN junction the CAR process is accompanied by the unintended EC process. Since the CAR and EC processes transfer opposite charge carriers, the measurable signal of the CAR process is masked or even completely canceled by that of the EC process. Moreover, the appearance of the EC process deeply suppresses the CAR

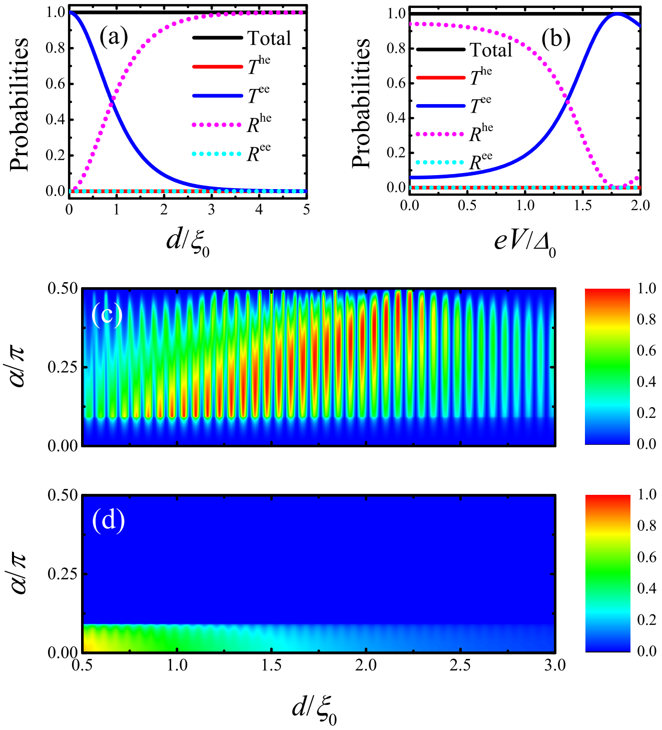

FIG. 2. Scattering probabilities versus (a) the junction length d and (b) bias voltage V for the normal incidence (i.e., $\alpha = 0$), where $eV = 0.5\Delta_0$ in (a) and $d = 2.1\xi_0$ in (b). Panels (c) and (d) present the contour plots of probabilities $T^{\rm he}$ and $T^{\rm ee}$, respectively, where $eV = 0.9\Delta_0$. In all panels, $\mu_L = -\mu_R = 0.5\Delta_0$, $Z_L = Z_R = 0$. The incident angle $\alpha = \arctan(k_\parallel/k^e_{L,z})$ and ξ_0 symbolizes the superconducting coherence length.

transport. Additionally, the signal of CAR transport can also be weakened by the LAR process. Therefore, to improve the efficiency and measurability of the Cooper-pair splitting, both the EC and LAR processes need to be forbidden. By virtue of the zero momentum of the Weyl node, we demonstrate that both the EC and LAR processes can be totally suppressed by properly tuning the chemical potentials μ_L and μ_R, resulting in an exclusive CAR transport. The underlying mechanism can be understood resorting to the scattering configurations. To do so, we assume the chemical potentials of the L and R regions take the relation of $\mu_L = -\mu_R \equiv \mu \geqslant 0$. As a consequence, the scattering angles satisfy $\alpha^e_L = \alpha^h_R \equiv \alpha$ and $\alpha^h_L = \alpha^e_R \equiv \alpha'$. Here the incident angle is chosen as α, and the scattering angles of NR (LAR) and EC (CAR) processes are, respectively, parametrized by $\alpha^{e(h)}_L$ and $\alpha^{e(h)}_R$. According to the conservation of $k_\parallel$, we have $(\varepsilon + \mu)\sin\alpha = (\varepsilon - \mu)\sin\alpha'$. Since $(\varepsilon + \mu) \geqslant |\varepsilon - \mu|$ for $\varepsilon > 0$, there exists a critical incident angle $\alpha_c = \arcsin[|eV - \mu|/(eV + \mu)]$ [36,38,44]. For an electronlike incident quasiparticle with energy $\varepsilon \geqslant 0$ and incident angle $|\alpha| > \alpha_c$, the LAR and EC processes are completely suppressed. Consequently, the nonlocal transport is solely contributed by the CAR process, leading to an exclusive CAR transport. This scenario is quantitatively illustrated in Figs. 2(c) and 2(d), where $\alpha_c \simeq 0.09\pi$. As can be seen, for $\alpha > 0.09\pi$, the exclusive CAR probability T^{he} with a sufficiently large value can be achieved. However, for $\alpha < 0.09\pi$, T^{he} is deeply suppressed, and the nonlocal transport is dominated by the EC process.

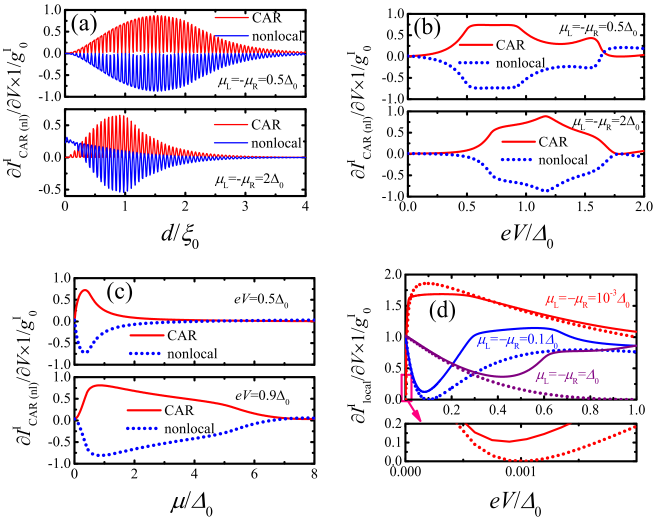

FIG. 3. Panels (a), (b), and (c) present, respectively, the dependence of nonlocal differential conductance on junction length d, bias voltage V, and chemical potential μ, where $eV = 0.5\Delta_0$ in (a) and $d = 2.1\xi_0$ in (b) and (c). In panel (c), the chemical potentials in the L and R WSM regions satisfy $\mu_L = -\mu_R = \mu$. Panel (d) gives the dependence of local differential conductance on the bias voltage, where the solid and short-dotted curves correspond to $d = 2.1\xi_0$ and $d = 10\xi_0$, respectively. In all panels, $Z_L = Z_R = 0$.

The proposed scattering configurations also manifest themselves in the experimentally measurable CAR and nonlocal differential conductances, as shown in Fig. 3. Especially, as elucidated above, for $\mu_L = -\mu_R = eV$ the critical angle $\alpha_c = 0$, implying that the LAR and EC processes are forbidden for all possible incident angles. Consequently, the nonlocal differential conductance is exclusively contributed by the CAR process, i.e., $\partial I^{\rm I}_{nl}/\partial V = -\partial I^{\rm I}_{\rm CAR}/\partial V$, as depicted by the upper panels in Figs. 3(a)–3(c). As regards the d-dependent CAR conductance, one can find that the maximum is achieved when d is comparable with the superconducting coherence length ξ_0. This is because, on the one hand, for $d \lesssim \xi_0$ the EC process dominates the nonlocal transport and suppresses the CAR process. On the other hand, since the quasiparticles in the S region are evanescent for $eV < \Delta_0$, the nonlocal transport processes are exponentially suppressed for a sufficiently large d [see Fig. 3(a) for details]. Most saliently, the CAR-dominated nonlocal transport can be realized within wide ranges of bias voltage V and chemical potential μ, as can be seen in Figs. 3(b) and 3(c). Intriguingly, the eV-dependent CAR and nonlocal differential conductances exhibit plateaus for $\mu_L = -\mu_R = 0.5\mu$. These scenarios indicate that the exclusive CAR conductance is not strongly dependent on the bias voltage, which should be favorable for the experimental realization. In addition, we note that in a similar graphene-based NSN junction [36] the eV-dependent CAR conductance just possesses a tip at $eV = \mu_L = -\mu_R$, which means that the CAR-dominated nonlocal transport is sensitive to the bias voltage and is difficult to be realized in practice. In this regard,

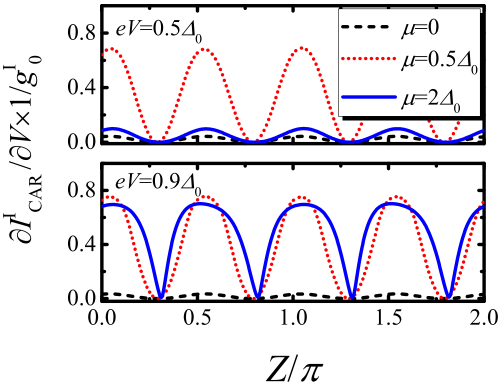

FIG. 4. The interfacial-barrier-strength-dependent differential conductance for the CAR process, where $d = 2.1\xi_0$, $Z_L = Z_R = Z$, and $\mu_L = \mu_R = \mu$.

the proposed type-I WSM-based NSN junction should be more interesting for realizing the exclusive CAR transport.

To perform a comparison of local transport properties in type-I WSM-based NSN and NS junctions, we consider the local differential conductance in the proposed type-I WSM-based NSN junction. As illustrated in Fig. 3(d), for $d = 10\xi_0 \gg \xi_0$ the behaviors of local transport tend to those in a type-I WSM-based NS junction [26], namely, in the subgap energy regime (i.e., $eV < \Delta_0$) the local differential conductance disappears at $eV = \mu_L = -\mu_R$, as indicated by the short-dotted curves. This feature can be quantitatively analyzed as follows. On the one hand, the critical angle $\alpha_c = 0$ at $eV = \mu_L = -\mu_R$, leading to the disappearances of LAR and EC processes, i.e., $R^{he} = 0$ and $T^{ee} = 0$. On the other hand, since the quasiparticles in the S region are evanescent in the subgap regime, the nonlocal scattering probabilities T^{he} and T^{ee} vanish for $d = 10\xi_0 \gg \xi_0$, resulting in $R^{ee} = 1 - R^{he}$. According to Eq. (12), the integrand $1 - R^{ee} + R^{he} = 2R^{he} = 0$, leading to a vanishing local differential conductance. However, in the NSN junction with a small junction length, although the LAR and EC processes are prohibited when $eV = \mu_L = -\mu_R$, the CAR probability T^{he} is finite and $R^{ee} + T^{he} = 1$. Therefore, $1 - R^{ee} + R^{he} = T^{he}$ is finite and the nonlocal differential conductance is nonvanishing at $eV = \mu_L = -\mu_R$ [see the solid curves in Fig. 3(d) for details].

Figure 4 presents the dependence of CAR conductance on the strength of the interfacial barrier; it is observed that the CAR conductance oscillates with the barrier strength Z without a decaying profile. As proposed in Ref. [26], this property can be attributed to the spin/orbital-momentum locking of type-I WSMs. Notably, the nondecaying profile of CAR conductance makes the type-I WSM-based NSN junction favorable for the realization of Cooper-pair splitting.

III. TYPE-II WSM-BASED NSN JUNCTION

In this section, we concentrate on the effects of the anisotropic band structures on the nonlocal transport properties of type-II WSM-based NSN junctions. The proposed setup is similar to the type-I WSM-based NSN junction depicted in Fig. 1, except that the type-II WSM-based NSN junction is deposited in the xy plane and is assumed to be infinite in the yz plane. The superconducting correlation in the S region can be induced by a superconducting electrode via the proximity effect, as has been experimentally proposed in a type-II WSM-based SHS [21].

A. Model and formalism

We consider a NSN junction based on a time-reversal symmetric type-II WSM. Near the Weyl node Q, the single-particle effective Hamiltonian of a time-reversal symmetric type-II WSM can be written as $\hat{h}^{\mathrm{II}}_{+}(k) = \hbar v_1 k_x \hat{\sigma}_0 + \hbar v_2 k \cdot \hat{\boldsymbol{\sigma}}$, where v_2 denotes the Fermi velocity, $\hat{\boldsymbol{\sigma}} = (\hat{\sigma}_1, \hat{\sigma}_2, \hat{\sigma}_3)$ are Pauli matrices, and $k = (k_x, k_y, k_z)$ symbolize the momenta measured with respect to the Weyl node. The parameter v_1 depicts the tilting of the Weyl cone along the x direction, and $|v_1/v_2| > 1$ in accordance with the definitions of type-II WSMs. For definiteness, we set $v_1 > v_2 > 0$ hereafter.

To highlight the effects of the strongly anisotropic band structures on the nonlocal transport properties, we concentrate on a type-II WSM-based NSN junction extended along the $\mathbf{n}$ direction, where $\mathbf{n} = (\cos\gamma, \sin\gamma)$ indicates the normal directions of NS interfaces, and γ represents the interface orientation angle between directions of the x axis and $\mathbf{n}$. In this way, the two NS interfaces are located at $x = -y\tan\gamma$ and $x = -y\tan\gamma + d/\cos\gamma$, respectively. It is convenient to take a coordinate transformation of $(\tilde{x}, \tilde{y})^T = \hat{\mathbb{R}}(x, y)^T$, with the rotation operator $\hat{\mathbb{R}} = e^{i\sigma_2\gamma}$. In the new coordinate system, the L and R regions are, respectively, placed within ranges of $\tilde{x} < 0$ and $\tilde{x} > d$, and the S region is deposited within the range of $0 < \tilde{x} < d$. After the coordinate transformation, the single-particle effective Hamiltonian near the Weyl node Q can be recast into $\hat{h}^{\mathrm{II}}_{+}(\tilde{k}) = \hbar v_1 \hat{\sigma}_0(-i\partial_{\tilde{x}}\cos\gamma - \tilde{k}_y \sin\gamma) + \hbar v_2 \hat{\sigma}_1(-i\partial_{\tilde{x}}\cos\gamma - \tilde{k}_y\sin\gamma) + \hbar v_2\hat{\sigma}_2(-i\partial_{\tilde{x}}\sin\gamma + \tilde{k}_y\cos\gamma)$. For simplicity, we fix $k_z = 0$ throughout this work, as has been implemented in Refs. [27,28]. In the superconducting region we consider the Bardeen-Cooper-Schrieffer pairing which couples electron excitations near the Weyl node Q and hole excitations close to the Weyl node $-Q$. In the basis of $\psi = (\psi_{Q,\uparrow}, \psi_{Q,\downarrow}, \psi^*_{-Q,\downarrow}, -\psi^*_{-Q,\uparrow})^T$ the BdG Hamiltonian can be formulated as [27,28]

$$\mathcal{H}_{\mathrm{II}} = \begin{pmatrix} \hat{h}^{\mathrm{II}}_{+}(\tilde{k}) - \mu(\tilde{x}) & \hat{\Delta}(\tilde{x}) \\ \hat{\Delta}^{\dagger}(\tilde{x}) & -h^{\mathrm{II}}_{+}(\tilde{k}) + \mu(\tilde{x}) \end{pmatrix}. \quad (13)$$

Taking advantage of the step function model [26–31,33–44], the chemical potential can be parametrized as $\mu(\tilde{x}) = \mu_L\Theta(-\tilde{x}) + \mu_S\Theta(\tilde{x})\Theta(d - \tilde{x}) + \mu_R\Theta(\tilde{x} - d)$. As proposed in Sec. II A, the chemical potential of the S region is assumed to be large enough, so that the leakage of Cooper pairs is negligibly small [43,44]. Consequently, the pair potential can be rationally characterized by a step function model, i.e., $\hat{\Delta}(\tilde{x}) = \Delta_0\hat{\sigma}_0 e^{i\varphi}\Theta(\tilde{x})\Theta(d - \tilde{x})$.

In the L and R regions, by diagonalizing the BdG Hamiltonian straightforwardly, the dispersion relations can be written as

$$\varepsilon^{e(h)}_{j,\eta} = +(-)\hbar v_1(\tilde{k}_{j,x}\cos\gamma - \tilde{k}_y\sin\gamma) + \eta\hbar v_2|\tilde{k}_j| - (+)\mu_j, \quad (14)$$

where $\eta = \pm 1$, $|\tilde{k}_j| = \sqrt{\tilde{k}_{j,x}^2 + \tilde{k}_y^2}$, the superscript $e(h)$ represents the electronlike (holelike) band, and $j = L(R)$ denotes the related quantities of the L (R) region. It can be inferred that the Weyl cones tilt both in the $\tilde{x}$ and $\tilde{y}$ directions. According to Eq. (14), the group velocities along the $\tilde{x}$ direction can be formulated as

$$\begin{aligned}\tilde{v}_{j,x}^{e(h)} &\equiv \partial\varepsilon_j^{e(h)}/\partial(\hbar\tilde{k}_{j,x})\\ &= +(-)v_1\cos\gamma + \eta v_2\tilde{k}_{j,x}/|\tilde{k}_j|,\end{aligned} \tag{15}$$

depending on the interface orientation angle γ. Specifically, in the case of $v_1\cos\gamma > v_2$, $\tilde{v}_{j,x}^{e(h)}$ are always positive (negative). Consequently, in the two N regions, all electronlike (holelike) quasiparticles propagate along the $+(-)\tilde{x}$ direction, resulting in so-called double EC (LAR) processes. Whereas, for $v_1\cos\gamma < v_2$, the scattering problem is similar to that of type-I WSM-based NSN junctions. Therefore, there are two essentially different scattering configurations which need to be considered separately.

Parenthetically, since the Fermi surfaces of type-II WSMs possess hyperbolalike profiles, the incident angle of an electron quasiparticle should be defined as $\theta = -\arctan(\tilde{v}_{L,y}^e/\tilde{v}_{L,x}^e)$, which is not identical to $-\arctan(\tilde{k}_y/\tilde{k}_{L,x}^e)$, as elaborated in Ref. [27]. Furthermore, the range of θ should be restricted in accordance with the following considerations. On the one hand, it can be inferred from Eq. (14) that, for a given γ, the incident angle θ should satisfy the relation of $|\sin(\theta-\gamma)| \leqslant v_2/v_1$. On the other hand, since in this work we are only concerned with the current flowing though the NSN junctions along the x direction, the relation of $-\pi/2 < \theta < \pi/2$ should be satisfied. Combining the two conditions, we arrive at $\max(-\pi/2, \gamma-\theta_c) \leqslant \theta \leqslant \min(\pi/2, \gamma+\theta_c)$, with θ_c being defined as $\theta_c = \arcsin(v_2/v_1)$.

1. $v_1\cos\gamma > v_2$

In the L region ($\tilde{x} < 0$), there are two possible electronlike incident quasiparticles stemming from the $\varepsilon_{L,-}^e$ and $\varepsilon_{L,+}^e$ bands, respectively, which can only be Andreev reflected as holelike quasiparticles. Consequently, the corresponding wave functions are, respectively, given by

$$\tilde{\Psi}_{L,-} = \tilde{\psi}_{L,1}^e + \tilde{r}_{1,-}^{he}\tilde{\psi}_{L,1}^h + \tilde{r}_{2,-}^{he}\tilde{\psi}_{L,2}^h, \tag{16a}$$

$$\tilde{\Psi}_{L,+} = \tilde{\psi}_{L,2}^e + \tilde{r}_{1,+}^{he}\tilde{\psi}_{L,1}^h + \tilde{r}_{2,+}^{he}\tilde{\psi}_{L,2}^h, \tag{16b}$$

where the amplitudes of LAR processes are symbolized by $\tilde{r}_{i,\pm}^{he}$ ($i = 1, 2$) and the basis scattering states $\tilde{\psi}_{1,2}^{e,h}$ are given by Eq. (B1). In the R region, since only electronlike quasiparticles propagate along the $+\tilde{x}$ direction for $v_1\cos\gamma > v_2$, the CAR process disappears and only the two EC processes arise. Accordingly, the wave functions of the R region ($\tilde{x} > d$) can be written as

$$\tilde{\Psi}_{R,-} = \tilde{t}_{1,-}^{ee}\psi_{R,1}^e + \tilde{t}_{2,-}^{ee}\psi_{R,2}^e, \tag{17a}$$

$$\tilde{\Psi}_{R,+} = \tilde{t}_{1,+}^{ee}\psi_{R,1}^e + \tilde{t}_{2,+}^{ee}\psi_{R,2}^e, \tag{17b}$$

with $\tilde{t}_{i,\pm}^{ee}$ the corresponding transmission amplitudes for the EC processes. In the S region ($0 < \tilde{x} < d$), the wave function $\tilde{\Psi}_S$ is a linear superposition of all possible basis scattering states, viz.,

$$\tilde{\Psi}_S = \sum_{m=1}^{4}\tilde{s}_m\tilde{\psi}_m^S, \tag{18}$$

where $\tilde{s}_m$ labels the related scattering coefficients, and the details of $\tilde{\psi}_m^S$ are shown in Eq. (B3).

The effects of interfacial imperfections can be modeled by two interfacial barriers arranged in the regions of $-d_L/2 < \tilde{x} < d_L/2$ and $-d_R/2 + d < \tilde{x} < d_R/2 + d$, with strengths U_L and U_R, respectively. As proposed in Sec. II A, we take the limits of $U_{L(R)} \to \infty$ and $d_{L(R)} \to 0$ with $U_{L(R)}d_{L(R)}/(\hbar v_2) \equiv \tilde{Z}_{L(R)}$ being finite. In the barrier regions, the corresponding wave functions are linear superpositions of all possible basis scattering states, taking forms of

$$\tilde{\Psi}_{BL} = \tilde{b}_1\tilde{\psi}_{B,L,1}^e + \tilde{b}_2\tilde{\psi}_{B,L,2}^e + \tilde{b}_3\tilde{\psi}_{B,L,1}^h + \tilde{b}_4\tilde{\psi}_{B,L,2}^h, \tag{19a}$$

$$\tilde{\Psi}_{BR} = \tilde{c}_1\tilde{\psi}_{B,R,1}^e + \tilde{c}_2\tilde{\psi}_{B,R,2}^e + \tilde{c}_3\tilde{\psi}_{B,R,1}^h + \tilde{c}_4\tilde{\psi}_{B,R,2}^h, \tag{19b}$$

where $\tilde{b}_m$ and $\tilde{c}_m$ label the related scattering amplitudes, and the detailed structures of basis scattering states are given in Appendix B 1.

As proposed in Sec. II A, the scattering amplitudes can be obtained by demanding the continuities of wave functions at the boundaries. With this in hand, the probabilities for the LAR processes can be defined as

$$\tilde{R}_{1(2),-}^{he} = \left|\frac{\langle\tilde{\psi}_{L,1(2)}^h|\mathcal{J}_{\tilde{x}}^{\mathrm{II}}|\tilde{\psi}_{L,1(2)}^h\rangle}{\langle\tilde{\psi}_{L,1}^e|\mathcal{J}_{\tilde{x}}^{\mathrm{II}}|\tilde{\psi}_{L,1}^e\rangle}\right||\tilde{r}_{1(2),-}^{he}|^2, \tag{20a}$$

$$\tilde{R}_{1(2),+}^{he} = \left|\frac{\langle\tilde{\psi}_{L,1(2)}^h|\mathcal{J}_{\tilde{x}}^{\mathrm{II}}|\tilde{\psi}_{L,1(2)}^h\rangle}{\langle\tilde{\psi}_{L,2}^e|\mathcal{J}_{\tilde{x}}^{\mathrm{II}}|\tilde{\psi}_{L,2}^e\rangle}\right||\tilde{r}_{1(2),+}^{he}|^2, \tag{20b}$$

where the particle current density operator $\mathcal{J}_{\tilde{x}}^{\mathrm{II}} = \frac{-i}{\hbar}[\tilde{x}, \mathcal{H}_{\mathrm{II}}]$. According to Eq. (13), we have $\mathcal{J}_{\tilde{x}}^{\mathrm{II}} = \tau_3 \otimes (v_1\cos\gamma\sigma_0 + v_2\cos\gamma\sigma_1 + v_2\sin\gamma\sigma_2)$, with τ_3 the Pauli matrix operating on the Nambu space. For the EC processes, the transmission probabilities can be formulated as

$$\tilde{T}_{1(2),-}^{ee} = \left|\frac{\langle\psi_{R,1(2)}^e|\mathcal{J}_{\tilde{x}}^{\mathrm{II}}|\psi_{R,1(2)}^e\rangle}{\langle\psi_{L,1}^e|\mathcal{J}_{\tilde{x}}^{\mathrm{II}}|\psi_{L,1}^e\rangle}\right||\tilde{t}_{1(2),-}^{ee}|^2, \tag{21a}$$

$$\tilde{T}_{1(2),+}^{ee} = \left|\frac{\langle\psi_{R,1(2)}^e|\mathcal{J}_{\tilde{x}}^{\mathrm{II}}|\psi_{R,1(2)}^e\rangle}{\langle\psi_{L,2}^e|\mathcal{J}_{\tilde{x}}^{\mathrm{II}}|\psi_{L,2}^e\rangle}\right||\tilde{t}_{1(2),+}^{ee}|^2. \tag{21b}$$

Resorting to the transmission probabilities, the zero-temperature differential conductance for the EC process can be written as

$$\frac{\partial I_{\mathrm{EC}}^{\mathrm{II}}}{\partial V} = \sum_{i=1,2}\sum_{\delta=\pm}\frac{4e^2A}{h}\int\frac{d\tilde{\boldsymbol{k}}_{\parallel}}{(2\pi)^2}\tilde{T}_{i,\delta}^{ee}(eV, \tilde{k}_{\parallel})\Theta(v_1\cos\gamma - v_2), \tag{22}$$

where $\tilde{\boldsymbol{k}}_{\parallel} = (\tilde{k}_y, k_z)$ and $\tilde{k}_{\parallel} = |\tilde{\boldsymbol{k}}_{\parallel}|$. The parameter κ is the cut-off value of the integral area, satisfying $\kappa \geqslant \sqrt{\tilde{k}_y^2 + k_z^2}$.

Since the CAR process disappears for $v_1 \cos\gamma > v_2$, only the two EC processes contribute to the nonlocal transport. Therefore, the nonlocal differential conductance at zero temperature can be defined as $\partial I^{\rm II}_{nl}/\partial V = \partial I^{\rm II}_{\rm EC}/\partial V$. To normalize the differential conductance, it is advisable to define $\tilde g^{\rm II}_0(eV) = 4e^2\kappa^2 A/(\pi h)\Theta(v_1\cos\gamma - v_2)$. Additionally, taking advantage of the BTK formula [34], the local differential conductance at zero temperature can be formulated as

$$\frac{\partial I^{\rm II}_l}{\partial V} = \sum_{i=1,2}\sum_{\delta=\pm}\frac{4e^2A}{h}\int\frac{d\tilde{\boldsymbol k}_\parallel}{(2\pi)^2}\big[2+\tilde R^{he}_{i,\delta}(eV,\tilde k_\parallel)\big]\Theta(v_1\cos\gamma - v_2). \tag{23}$$

2. $v_1 \cos\gamma < v_2$

In the L region, we take an electronlike quasiparticle as the incident one, and the scenarios resulting from a holelike incident quasiparticle can be discussed in the same way. For an electronlike incident quasiparticle propagating along the $+\tilde{\boldsymbol x}$ direction, it can either be normally reflected as an electronlike quasiparticle or be Andreev reflected as a holelike one, thus the involved wave function can be formulated as

$$\tilde\Phi_L = \tilde\phi^e_{L,1} + \tilde r^{ee}\tilde\phi^e_{L,2} + \tilde r^{he}\tilde\phi^h_{L,2}, \tag{24}$$

where $\tilde r^{ee}$ and $\tilde r^{he}$, respectively, represent the scattering amplitudes for the NR and LAR processes. The basis scattering states $\tilde\phi^{e,h}_{j,1}$ and $\tilde\phi^{e,h}_{j,2}$ $(j = L, R)$ are given in Eq. (B6). The incident quasiparticle can also tunnel into the R region through the EC or CAR process. Thus, in the R region the wave function can be expressed as

$$\tilde\Phi_R = \tilde t^{ee}\tilde\phi^e_{R,1} + \tilde t^{he}\tilde\phi^h_{R,1}, \tag{25}$$

with $\tilde t^{ee}$ and $\tilde t^{he}$ the transmission amplitudes for the EC and CAR processes, respectively. In the two interfacial barrier regions, the wave functions can also be described by Eq. (19), by substituting $\tilde\psi^{e,h}_{B,j,1}$ and $\tilde\psi^{e,h}_{B,j,2}$ with $\tilde\phi^{e,h}_{B,j,1}$ and $\tilde\phi^{e,h}_{B,j,2}$, respectively. The details of $\tilde\phi^{e,h}_{B,j,1}$ and $\tilde\phi^{e,h}_{B,j,2}$ are presented in Appendix B 2. In the S region, the wave function is given by Eq. (18).

According to the standard procedure of matching corresponding wave functions at the boundaries, we can get the scattering amplitudes. In doing so, the probabilities for the NR and LAR processes can be, respectively, written as

$$\tilde R^{ee} = \left|\frac{\langle\tilde\phi^e_{L,2}|\mathcal{J}^{\rm II}_{\tilde x}|\tilde\phi^e_{L,2}\rangle}{\langle\tilde\phi^e_{L,1}|\mathcal{J}^{\rm II}_{\tilde x}|\tilde\phi^e_{L,1}\rangle}\right||\tilde r^{ee}|^2, \tag{26a}$$

$$\tilde R^{he} = \left|\frac{\langle\tilde\phi^h_{L,2}|\mathcal{J}^{\rm II}_{\tilde x}|\tilde\phi^h_{L,2}\rangle}{\langle\tilde\phi^e_{L,1}|\mathcal{J}^{\rm II}_{\tilde x}|\tilde\phi^e_{L,1}\rangle}\right||\tilde r^{he}|^2, \tag{26b}$$

for the EC and CAR processes, and the related probabilities are, respectively, given by

$$\tilde T^{ee} = \left|\frac{\langle\tilde\phi^e_{R,1}|\mathcal{J}^{\rm II}_{\tilde x}|\tilde\phi^e_{R,1}\rangle}{\langle\tilde\phi^e_{L,1}|\mathcal{J}^{\rm II}_{\tilde x}|\tilde\phi^e_{L,1}\rangle}\right||\tilde t^{ee}|^2, \tag{27a}$$

$$\tilde T^{he} = \left|\frac{\langle\tilde\phi^h_{R,1}|\mathcal{J}^{\rm II}_{\tilde x}|\tilde\phi^h_{R,1}\rangle}{\langle\tilde\phi^e_{L,1}|\mathcal{J}^{\rm II}_{\tilde x}|\tilde\phi^e_{L,1}\rangle}\right||\tilde t^{he}|^2. \tag{27b}$$

By virtue of the transmission probabilities, the zero-temperature differential conductances for the EC and CAR processes can be, respectively, defined as

$$\frac{\partial I^{\rm II}_{\rm EC}}{\partial V} = \frac{4e^2A}{h}\int\frac{d\tilde{\boldsymbol k}_\parallel}{(2\pi)^2}\tilde T^{ee}(eV,\tilde k_\parallel)\Theta(v_2 - v_1\cos\gamma), \tag{28a}$$

$$\frac{\partial I^{\rm II}_{\rm CAR}}{\partial V} = \frac{4e^2A}{h}\int\frac{d\tilde{\boldsymbol k}_\parallel}{(2\pi)^2}\tilde T^{he}(eV,\tilde k_\parallel)\Theta(v_2 - v_1\cos\gamma). \tag{28b}$$

Thus, the nonlocal differential conductance at zero temperature can be obtained as $\partial I^{\rm II}_{nl}/\partial V = \partial I^{\rm II}_{\rm EC}/\partial V - \partial I^{\rm II}_{\rm CAR}/\partial V$. To normalize the differential conductance, we define $\tilde g^{\rm II}_0(eV) = 2e^2\kappa^2 A/(\pi h)\Theta(v_2 - v_1\cos\gamma)$. Resorting to the BTK formula, the local differential conductance at zero temperature can be defined as

$$\frac{\partial I^{\rm II}_l}{\partial V} = \frac{4e^2A}{h}\int\frac{d\tilde{\boldsymbol k}_\parallel}{(2\pi)^2}[1 - \tilde R^{ee}(eV,\tilde k_\parallel) + \tilde R^{he}(eV,\tilde k_\parallel)] \times \Theta(v_2 - v_1\cos\gamma). \tag{29}$$

B. Results and discussion

We now proceed to analyze the numerical results and discuss the transport properties of type-II WSM-based NSN junctions. What we mainly focus on are the manifestations of the anisotropic band structures in the transport scenarios. For definiteness, the associated parameters are fixed as $v_1 = 2$, $v_2 = 1$, and $\mu_S = 100\Delta_0$ in the numerical calculation. In doing so, the critical interface orientation angle can be evaluated as $\gamma_c = \cos^{-1}(v_2/v_1) = \pi/3$. For $\gamma < \pi/3$, there only exist double LAR and double EC processes. Whereas, for $\gamma > \pi/3$, the scattering mechanism is similar to that in type-I WSM-based NSN junctions, as proposed in Sec. III A. In addition, the parameter $\theta_c = \pi/6$, thus the incident angle θ should be restricted within the range of $[\max(-\pi/2, \gamma - \pi/6), \min(\pi/2, \gamma + \pi/6)]$.

To uncover the influences of the anisotropic band structures on the scattering configurations, we investigate the incident-angle- and energy-dependent scattering probabilities for $\gamma = \pi/18$, and compare our findings with the results corresponding to $\gamma = 0$ [28]. As shown in Fig. 5, it is found that the EC probability $\tilde T^{ee}_{2,-}$ is almost independent of the incident angle θ, while the other three scattering probabilities, i.e., $\tilde R^{he}_{1,-}$, $\tilde R^{he}_{2,-}$, and $\tilde T^{ee}_{1,-}$, nonmonotonically vary with increasing θ. These results are independent of the incident energy. In contrast, as proposed in Ref. [28], in the case of $\gamma = 0$, for a fixed incident energy all the scattering probabilities monotonically depend on the incident angle. The clear-cut difference between the scattering configurations of $\gamma = \pi/18$ and $\gamma = 0$ reflects the anisotropic aspects of type-II WSMs. It is worthy stressing that the remarkable γ-dependent scattering configurations are unique for the type-II WSMs, which are absent in similar NSN junctions based on other Dirac materials [36–43]. In addition, by inspecting the scattering probabilities related to junction lengths $d = \xi_0$ and $d = 5\xi_0$, one can find that the tunneling resonances appear in the long NSN junction with length $d = 5\xi_0$, and thus enhance the amplitudes of scattering probabilities. Furthermore, the proposed resonant peaks can

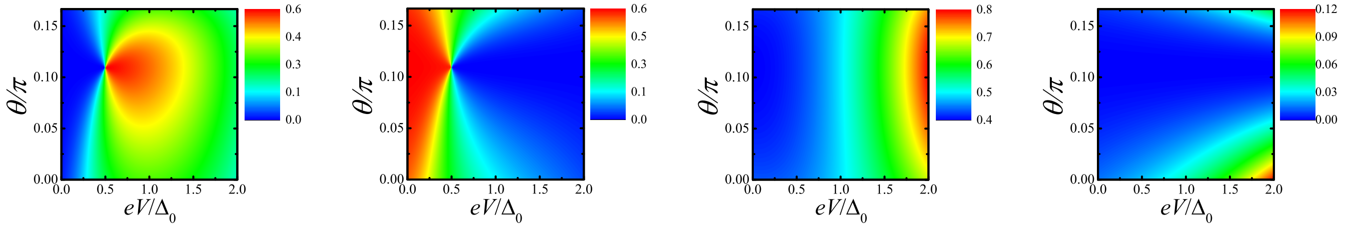

(a)$\tilde{R}^{he}_{1,-}$, $d=\xi_0$ (b)$\tilde{R}^{he}_{2,-}$, $d=\xi_0$ (c)$\tilde{T}^{ee}_{1,-}$, $d=\xi_0$ (d)$\tilde{T}^{ee}_{2,-}$, $d=\xi_0$

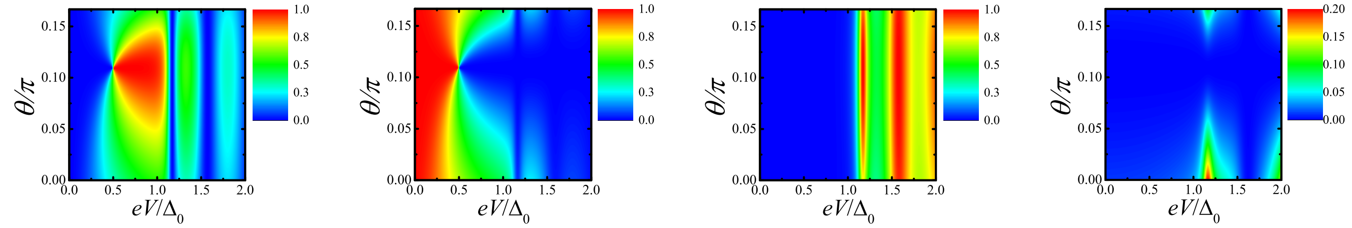

(e)$\tilde{R}^{he}_{1,-}$, $d=5\xi_0$ (f)$\tilde{R}^{he}_{2,-}$, $d=5\xi_0$ (g)$\tilde{T}^{ee}_{1,-}$, $d=5\xi_0$ (h)$\tilde{T}^{ee}_{2,-}$, $d=5\xi_0$

FIG. 5. Contour plots of the scattering probabilities versus the incident angle θ and energy eV, where the incident mode is selected as $\tilde{\psi}^{e}_{L,1}$. In all panels, $\gamma=\pi/18$, $\mu_L=\mu_R=0.5\Delta_0$, and $\tilde{Z}_L=\tilde{Z}_R=0$.

be achieved by electrically tuning the bias voltage, as indicated by panels (d)–(h) in Fig. 5.

We now turn to the manifestations of anisotropic band structures in the experimentally measurable conductance. The contour plots of nonlocal differential conductance are illustrated in Fig. 6. In all panels, one can find that the nonlocal differential conductance strongly depends on γ. Specifically, as can be seen in Fig. 6(a), for $eV \gtrsim \Delta_0$, the oscillation period ($\mathcal{T}$) of the eV-dependent nonlocal differential conductance obviously varies with γ, quite differing from that in similar NSN junctions based on graphene [38] and topological insulators [39]. This phenomenon can be quantitatively understood as follows. Actually, in the regime of $\mu_S \gg \Delta_0$, the oscillation period $\mathcal{T} \propto \frac{\hbar|v_1^2\cos^2\gamma - v_2^2|}{2\mu_S v_2}$. Accordingly, for a set of fixed $v_1=2$ and $v_2=1$, one can find that $\mathcal{T}$ decays by enhancing γ within the range of $[0,\pi/3]$ and increases when γ changes from $\pi/3$ to $\pi/2$. Figure 6(b) depicts the zero-bias nonlocal differential conductance as functions of γ and d. It is found that with increasing d, the nonlocal differential conductance monotonically decays in the case of $\gamma<\pi/3$. As mentioned in Ref. [28], this scenario results from the phase difference of π between the two d-dependent transmission probabilities, i.e., $\tilde{T}^{ee}_{1,+(-)}(d)$ and $\tilde{T}^{ee}_{1,+(-)}(d)$, which dismisses the oscillating textures of the d-dependent zero-bias nonlocal differential conductance. Notably, although in Ref. [28] the proposed mechanism was concluded by analyzing the scattering configurations of $\gamma=0$, our findings reveal that the validity of the mechanism can be extended to the situations of $0<\gamma<\pi/3$. Additionally, for $\gamma>\pi/3$, the scattering configurations are similar to that in similar NSN junctions based on other Dirac systems [36,38–43], and the d-dependent nonlocal differential conductance harbors oscillating characters when d is not sufficiently large. By passing, the decaying profile of d-dependent nonlocal differential conductance originates from the evanescent characters of the modes in the superconducting region. The γ-dependent behaviors of the zero-bias nonlocal differential conductance can also be observed in Figs. 6(c) and 6(d). In the regime of $\gamma<\pi/3$, the nonlocal differential conductance is independent of the chemical potential μ and the interfacial barrier strength $\tilde{Z}$. However, for $\gamma>\pi/3$, the nonlocal differential conductance slightly decays with increasing the chemical potential, and the $\tilde{Z}$-dependent nonlocal differential conductance exhibits tiny oscillating textures. The γ-dependent nonlocal differential conductance can be ascribed to the anisotropic aspects of type-II WSMs. In the case of $\gamma<\pi/3$, the band structures in the two N regions are overtilted, so that both the NR and CAR processes are completely suppressed, and the nonlocal transport is solely contributed by the EC process. Whereas, for $\gamma>\pi/3$, the band tilting is weakened, and both the CAR and EC processes

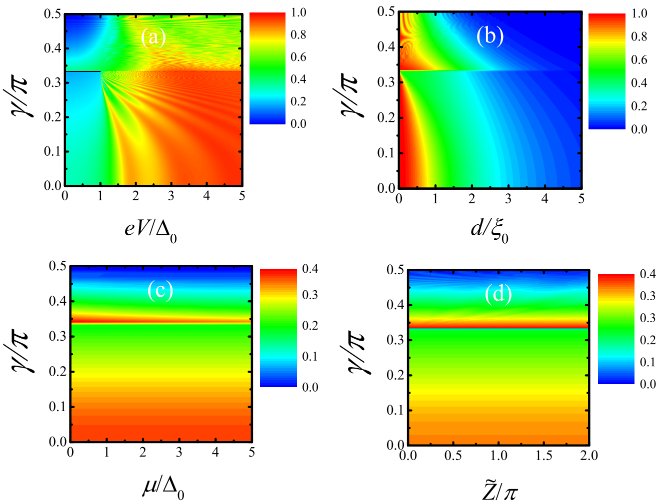

FIG. 6. Contour plots of nonlocal differential conductance $\partial I^{\rm II}_{nl}/\partial V \times 1/\tilde{g}^{\rm II}_0$. The related parameters are taken as (a) $d=2\xi_0$, $\mu_L=\mu_R=0.5\Delta_0$, and $\tilde{Z}_L=\tilde{Z}_R=0$; (b) $eV=0$, $\tilde{Z}_L=\tilde{Z}_R=0$, and $\mu_L=\mu_R=0.5\Delta_0$; (c) $d=2\xi_0$, $eV=0$, $\tilde{Z}_L=\tilde{Z}_R=0$, and $\mu_L=\mu_R=\mu$; (d) $\tilde{Z}_L=\tilde{Z}_R\equiv\tilde{Z}$, $d=2\xi_0$, $\mu_L=\mu_R=0.5\Delta_0$, and $eV=0$.

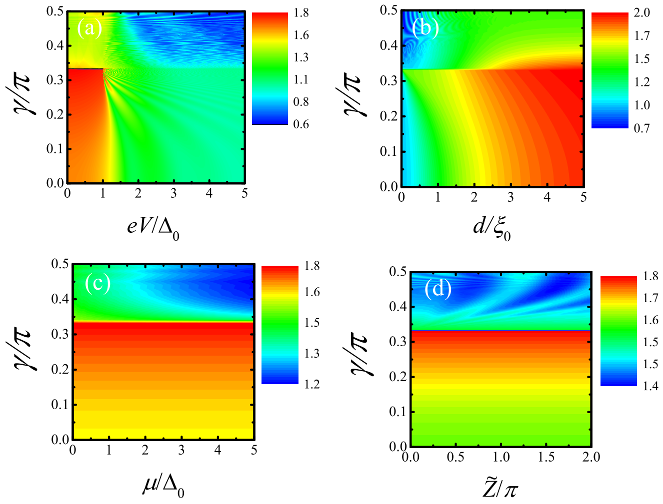

FIG. 7. Contour plot of the local differential conductance $\partial I_l^{\mathrm{II}}/\partial V \times 1/\tilde{g}_0^{\mathrm{II}}$. The related parameters are taken as (a) $d = 2\xi_0$, $\mu_L = \mu_R = 0.5\Delta_0$, and $\tilde{Z}_L = \tilde{Z}_R = 0$; (b) $eV = 0$, $\mu_L = \mu_R = 0.5\Delta_0$, and $\tilde{Z}_L = \tilde{Z}_R = 0$; (c) $d = 2\xi_0$, $eV = 0$, $\tilde{Z}_L = \tilde{Z}_R = 0$, and $\mu_L = \mu_R = \mu$; (d) $\tilde{Z}_L = \tilde{Z}_R \equiv \tilde{Z}$, $d = 2\xi_0$, $\mu_L = \mu_R = 0.5\Delta_0$, and $eV = 0$.

contribute to the nonlocal differential conductance. We note that the nonlocal differential conductance is always positive even in the regime of $\gamma > \pi/3$, implying that the EC process dominates the nonlocal transport in type-II WSM-based NSN junctions. Moreover, the exclusive CAR transport is absent in type-II WSM-based NSN junctions. This scenario can be attributed to the fact that the electron and hole pockets coexist in the neighborhood of the Fermi level and both contribute to the nonlocal transport.

Besides the nonlocal differential conductance discussed above, we now investigate the local differential conductance in a type-II WSM-based NSN junction. As shown in Fig. 7(a), in the case of $eV \gtrsim \Delta_0$, the local differential conductance decays with increasing eV and possesses oscillating textures. Moreover, the oscillation period of the eV-dependent local differential conductance also depends on γ. As can be seen, with increasing γ the oscillation period of the eV-dependent local differential conductance decreases within the range of $\gamma < \pi/3$ and increases when $\gamma > \pi/3$. The oscillating textures originate from the quantum interferences due to the multi-interface geometry of the proposed NSN junction, which are absent in the type-II WSM-based NS junction [27]. As shown in Ref. [27], in the situation of $eV \gtrsim \Delta_0$, the local differential conductance monotonically decreases with increasing eV. In the subgap regime, i.e., $eV \lesssim \Delta_0$, with enhancing γ the local differential conductance monotonically increases in the regime of $\gamma < \pi/3$ and slightly oscillates with γ when $\gamma > \pi/3$. These characters are also different from those in a type-II WSM-based NS junction [27], where the γ-dependent zero-bias local differential conductance exhibits a plateau for $\gamma < \pi/3$ and monotonically decays when γ changes from $\pi/3$ to $\pi/2$. The dependence of zero-bias local differential conductance on d is depicted in Fig. 7(b). It is observed that in the regime of $\gamma < \pi/3$ the zero-bias local differential conductance can be smoothly enhanced by increasing d, while in the case of $\gamma > \pi/3$ the zero-bias local differential conductance possesses oscillating characters for small d. Furthermore, by inspecting Figs. 6(c) and 6(d), one can find that the zero-bias local differential conductance oscillates with μ and $\tilde{Z}$ when $\gamma > \pi/3$. With regard to $\gamma < \pi/3$, the zero-bias local differential conductance is insensitive to both μ and $\tilde{Z}$. In light of the above elucidations, one can conclude that in the type-II WSM-based NSN junction the local differential conductance is also γ dependent and different from that in a type-II WSM-based NS junction.

IV. CONCLUSION

To conclude, we have investigated transport properties in NSN junctions based on time-reversal symmetric type-I and type-II WSMs. In contrast to those in similar NSN junctions based on other Dirac materials, in the proposed type-I WSM-based NSN junction the CAR transport probability vanishes for normal incidence. Remarkably, a CAR-dominated nonlocal differential conductance can be achieved within wide ranges of related parameters. Additionally, owing to the spin/orbital-momentum locking of type-I WSMs, the proposed CAR-dominated nonlocal differential conductance possesses a nondecaying profile with enhancing the strengths of interfacial barriers. These intriguing attributes enable the type-I WSM-based NSN junctions to be favorable for the Cooper-pair splitting.

For the type-II WSM-based NSN junction, the manifestations of the anisotropic aspects of type-II WSMs in the nonlocal transport have been emphasized. Due to the anisotropic band structures of the type-II WSM, the scattering configurations and nonlocal differential conductance are strongly dependent on the interface orientation angle, in contrast to those in similar NSN junctions based on other Dirac materials. Furthermore, for $\gamma < \gamma_c$ the differential conductance is insensitive to the chemical potential and the strength of the interfacial barrier, while for $\gamma > \gamma_c$ the differential conductance exhibits oscillating textures with respect to the relevant parameters. These findings provide intriguing insights into the correlated transport properties in WSM-based superconducting heterostructures.

ACKNOWLEDGMENTS

H.L. would like to thank M. Wang, R. Wang, M. X. Chen, F. Tang, and S. Liang for illuminating discussions. This work was supported by the National Natural Science Foundation of China (Grants No. 11574080, No. 11804091, and No. 91833302) and the Natural Science Foundation of Hunan Province (Grant No. 2019JJ50380).

APPENDIX A: CALCULATION OF THE BASIS SCATTERING STATES IN A TYPE-I WSM-BASED NSN JUNCTION

In this Appendix we present necessary calculation details regarding the wave functions and related quantities in atype-I WSM-based NSN junction.

In the superconducting region, solving the BdG equation $\mathcal{H}_{\rm I}\psi = \varepsilon\psi$ straightforwardly yields

$$\psi^S_{1(2)} = \begin{pmatrix} k_\parallel e^{i\beta - i\eta} \\ [\mu_S + \Omega - (+)k^S_{z,1}]e^{i\beta} \\ k_\parallel e^{-i\varphi - i\eta} \\ [\mu_S + \Omega - (+)k^S_{z,1}]e^{-i\varphi} \end{pmatrix} e^{ik^S_{z,1(2)}z}, \tag{A1a}$$

$$\psi^S_{3(4)} = \begin{pmatrix} k_\parallel e^{i\varphi - i\eta} \\ [\mu_S - \Omega - (+)k^S_{z,2}]e^{i\varphi} \\ k_\parallel e^{i\beta - i\eta} \\ [\mu_S - \Omega - (+)k^S_{z,2}]e^{i\beta} \end{pmatrix} e^{ik^S_{z,3(4)}z}, \tag{A1b}$$

where $k^S_{z,2(4)} = -k^S_{z,1(3)}$, $\eta = \tan^{-1}(k_y/k_x)$, and the related parameters are

$$\Omega = i\sqrt{\Delta_0^2 - \varepsilon^2}\Theta(\Delta_0 - |\varepsilon|) + \text{sgn}(\varepsilon)\sqrt{\varepsilon^2 - \Delta_0^2}\Theta(|\varepsilon| - \Delta_0), \tag{A2a}$$

$$\beta = \cos^{-1}[|\varepsilon|/\Delta_0)\Theta(\Delta_0 - |\varepsilon|] - i\cosh^{-1}(|\varepsilon|/\Delta_0)\Theta(|\varepsilon| - \Delta_0), \tag{A2b}$$

$$k^S_{z,1(3)} = \text{sgn}[\varepsilon + (-)\sqrt{\Delta_0^2 + [\mu_S + (-)k_\parallel]^2}]\sqrt{[\mu_S + (-)\Omega]^2/(\hbar v)^2 - k_\parallel^2}. \tag{A2c}$$

In the two N regions, the basis scattering states can be formulated as

$$\psi^e_{j,+(-)} = \begin{pmatrix} k_\parallel e^{-i\eta} \\ \varepsilon + \mu_j - (+)k^e_{j,z} \\ 0 \\ 0 \end{pmatrix} e^{+(-)ik^e_{j,z}z}, \tag{A3a}$$

$$\psi^h_{j,+(-)} = \begin{pmatrix} 0 \\ 0 \\ -k_\parallel e^{-i\eta} \\ \varepsilon - \mu_j + (-)k^h_{j,z} \end{pmatrix} e^{+(-)ik^h_{j,z}z}, \tag{A3b}$$

where $j = L$ (R) denotes the related quantities of the L (R) region.

APPENDIX B: CALCULATION OF THE BASIS SCATTERING STATES IN A TYPE-II WSM-BASED NSN JUNCTION

In this Appendix we perform calculation details for the basis scattering states and involved parameters in a type-II WSM-based NSN junction.

1. $v_1 \cos\gamma > v_2$

For $v_1\cos\gamma > v_2$, in the N regions the basis states can be formulated as

$$\tilde{\psi}^e_{j,1(2)} = \begin{pmatrix} -(+)\sqrt{(\tilde{k}^e_{j,x,1(2)})^2 + \tilde{k}_y^2} \\ (\tilde{k}^e_{j,x,1(2)} + i\tilde{k}_y)e^{i\gamma} \\ 0 \\ 0 \end{pmatrix} e^{i(\tilde{k}^e_{j,x,1(2)}\tilde{x} + \tilde{k}_y\tilde{y})}, \tag{B1a}$$

$$\tilde{\psi}^h_{j,1(2)} = \begin{pmatrix} 0 \\ 0 \\ +(-)\sqrt{(\tilde{k}^h_{j,x,1(2)})^2 + \tilde{k}_y^2} \\ (\tilde{k}^h_{j,x,1(2)} + i\tilde{k}_y)e^{i\gamma} \end{pmatrix} e^{i(\tilde{k}^h_{j,x,1(2)}\tilde{x} + \tilde{k}_y\tilde{y})}, \tag{B1b}$$

where the related parameters are given by

$$\tilde{k}^e_{j,x,1(2)} = \frac{\tilde{v}_1(\varepsilon + \tilde{\mu}_j) + (-)v_2\sqrt{(\varepsilon + \tilde{\mu}_j)^2 + \hbar^2(\tilde{v}_1^2 - v_2^2)\tilde{k}_y^2}}{\hbar(\tilde{v}_1^2 - v_2^2)}, \tag{B2a}$$

$$\tilde{k}^h_{j,x,1(2)} = \frac{-\tilde{v}_1(\varepsilon - \tilde{\mu}_j) - (+)v_2\sqrt{(\varepsilon - \tilde{\mu}_j)^2 + \hbar^2(\tilde{v}_1^2 - v_2^2)\tilde{k}_y^2}}{\hbar(\tilde{v}_1^2 - v_2^2)}, \tag{B2b}$$

where $j = L, R$, $\tilde{v}_1 = v_1\cos\gamma$, and $\tilde{\mu}_j = \mu_j + \hbar v_1 \sin\gamma\tilde{k}_y$.

In the interfacial barrier regions, by substituting μ_j with U_j into Eq. (B2), the expressions of $\tilde{k}^{e,h}_{B,j,x,1(2)}$ can be obtained. In Eq. (B1), by substituting $\tilde{k}^{e,h}_{j,x,1(2)}$ with $\tilde{k}^{e,h}_{B,j,x,1(2)}$, we can get the basis states $\tilde{\psi}^{e,h}_{B,j,1(2)}$ in the interfacial barrier regions.

In the S region, in the limit of $\mu_S \gg \max\{\mu_{L(R)}, \Delta_0, \varepsilon\}$, the basis states can be formulated as

$$\tilde{\psi}^S_{1(3)} = \begin{pmatrix} e^{-i\beta + i\varphi} \\ +(-)e^{-i\beta + i\varphi + i\gamma} \\ 1 \\ +(-)e^{i\gamma} \end{pmatrix} e^{i(\tilde{k}^S_{x,1(3)}\tilde{x} + \tilde{k}_y\tilde{y})}, \tag{B3a}$$

$$\tilde{\psi}^S_{2(4)} = \begin{pmatrix} e^{i\beta + i\varphi} \\ +(-)e^{i\beta + i\varphi + i\gamma} \\ 1 \\ +(-)e^{i\gamma} \end{pmatrix} e^{i(\tilde{k}^S_{x,2(4)}\tilde{x} + \tilde{k}_y\tilde{y})}, \tag{B3b}$$

where the related parameters are defined as

$$\tilde{k}^S_{x,1(2)} = \frac{\mu_S - (+)i\Delta_0\sin\beta}{\hbar(v_1\cos\gamma + v_2)}, \tag{B4a}$$

$$\tilde{k}^S_{x,3(4)} = \frac{\mu_S - (+)i\Delta_0\sin\beta}{\hbar(v_1\cos\gamma - v_2)}. \tag{B4b}$$

As an aside, we note that the basis scattering states $\tilde{\psi}^S_{1,3(2,4)}$ propagate along the $-(+)\tilde{x}$ direction for $|\varepsilon| > \Delta_0$. In the case of $|\varepsilon| < \Delta_0$, $\tilde{\psi}^S_{1,3(2,4)}$ describe the evanescent modes and decay exponentially as $\tilde{x} \to -\infty$ ($\tilde{x} \to +\infty$).

2. $v_1 \cos\gamma < v_2$

We now proceed to the derivations of basis scattering states and associated quantities in the case of $v_1 \cos\gamma < v_2$. In the N regions, the $\tilde{x}$ components of the momenta can be expressed as

$$\tilde{q}^{e}_{j,x,1(2)} = \frac{\tilde{v}_1(\varepsilon + \tilde{\mu}_j) - (+)\zeta_{j,e} v_2 \sqrt{(\varepsilon + \tilde{\mu}_j)^2 + \hbar^2 \left(\tilde{v}_1^2 - v_2^2\right)\tilde{k}_y^2}}{\hbar\left(\tilde{v}_1^2 - v_2^2\right)}, \tag{B5a}$$

$$\tilde{q}^{h}_{j,x,1(2)} = \frac{\tilde{v}_1(\tilde{\mu}_j - \varepsilon) + (-)\zeta_{j,h} v_2 \sqrt{(\varepsilon - \tilde{\mu}_j)^2 + \hbar^2 \left(\tilde{v}_1^2 - v_2^2\right)\tilde{k}_y^2}}{\hbar\left(\tilde{v}_1^2 - v_2^2\right)}, \tag{B5b}$$

where $\zeta_{j,e(h)} = \mathrm{sgn}[\tilde{\mu}_j + (-)\varepsilon]$. The basis scattering states can be formulated as

$$\tilde{\phi}^{e}_{j,1(2)} = \begin{pmatrix} \zeta_{j,e}\sqrt{(\tilde{q}^{e}_{j,x,1(2)})^2 + \tilde{k}_y^2} \\ (\tilde{q}^{e}_{j,x,1(2)} + i\tilde{k}_y)e^{i\gamma} \\ 0 \\ 0 \end{pmatrix} e^{i(\tilde{q}^{e}_{j,x,1(2)}\tilde{x} + \tilde{k}_y\tilde{y})}, \tag{B6a}$$

$$\tilde{\phi}^{h}_{j,1(2)} = \begin{pmatrix} 0 \\ 0 \\ \zeta_{j,h}\sqrt{(\tilde{q}^{h}_{j,x,1(2)})^2 + \tilde{k}_y^2} \\ (\tilde{q}^{h}_{j,x,1(2)} + i\tilde{k}_y)e^{i\gamma} \end{pmatrix} e^{i(\tilde{q}^{h}_{j,x,1(2)}\tilde{x} + \tilde{k}_y\tilde{y})}. \tag{B6b}$$

In the interfacial barrier regions, the basis states $\tilde{\phi}^{e,h}_{B,j,1(2)}$ can be achieved by substituting $\tilde{q}^{e,h}_{j,x,1(2)}$ with $\tilde{q}^{e,h}_{B,j,x,1(2)}$ into Eq. (B6), where $\tilde{q}^{e,h}_{B,j,x,1(2)}$ can be obtained by substituting μ_j with U_j into Eq. (B5).

In the S region, the basis scattering states can also be formulated by Eq. (B3), except that $\tilde{\psi}^{S}_{1,4(2,3)}$ denote the basis scattering states propagating along the $-(+)\tilde{x}$ direction for $|\varepsilon| > \Delta_0$.

[1] N. P. Armitage, E. J. Mele, and A. Vishwanath, Rev. Mod. Phys. **90**, 015001 (2018).

[2] X. Wan, A. M. Turner, A. Vishwanath, and S. Y. Savrasov, Phys. Rev. B **83**, 205101 (2011).

[3] A. A. Soluyanov, D. Gresch, Z. Wang, Q. S. Wu, M. Troyer, X. Dai, and B. A. Bernevig, Nature (London) **527**, 495 (2015).

[4] K. Koepernik, D. Kasinathan, D. V. Efremov, S. Khim, S. Borisenko, B. Büchner, and J. van den Brink, Phys. Rev. B **93**, 201101 (2016).

[5] A. A. Burkov and L. Balents, Phys. Rev. Lett. **107**, 127205 (2011).

[6] H. Weng, C. Fang, Z. Fang, B. A. Bernevig, and X. Dai, Phys. Rev. X **5**, 011029 (2015).

[7] G. Halász and L. Balents, Phys. Rev. B **85**, 035103 (2012).

[8] H. B. Nielsen and M. Ninomiya, Phys. Lett. **130**, 389 (1983).

[9] B. Q. Lv, H. M. Weng, B. B. Fu, X. P. Wang, H. Miao, J. Ma, P. Richard, X. C. Huang, L. X. Zhao, G. G. Chen, Z. Fang, X. Dai, T. Qian, and H. Ding, Phys. Rev. X **5**, 031013 (2015).

[10] S.-M. Huang, S.-Y. Xu, I. Belopolski, C.-C. Lee, G. Chang, B. K. Wang, N. Alidoust, G. Bian, M. Neupane, C. Zhang, S. Jia, A. Bansil, H. Lin, and M. Z. Hasan, Nat. Commun. **6**, 7373 (2015).

[11] I. Belopolski, S.-Y. Xu, D. S. Sanchez, G. Chang, C. Guo, M. Neupane, H. Zheng, C.-C. Lee, S.-M. Huang, G. Bian, N. Alidoust, T.-R. Chang, B. K. Wang, X. Zhang, A. Bansil, H.-T. Jeng, H. Lin, S. Jia, and M. Z. Hasan, Phys. Rev. Lett. **116**, 066802 (2016).

[12] Z. K. Liu, L. X. Yang, Y. Sun, T. Zhang, H. Peng, H. F. Yang, C. Chen, Y. Zhang, Y. F. Guo, D. Prabhakaran, M. Schimidt, Z. Hussain, S.-K. Mo, C. Felser, B. Yan, and Y. L. Chen, Nat. Mater. **15**, 27 (2016).

[13] S.-Y. Xu, N. Alidoust, I. Belopolski, Z. Yuan, G. Bian, T.-R. Chang, H. Zheng, V. N. Storcov, D. S. Sanchez, G. Chang, C. Zhang, D. Mou, Y. Wu, L. Huang, C.-C. Lee, S.-M. Huang, B. K. Wang, A. Bansil, H.-R. Jeng, T. Neupert, A. Kaminski, H. Lin, S. Jia, and M. Z. Hassan, Nat. Phys. **11**, 748 (2015).

[14] L. Huang, T. M. McCormick, M. Ochi, Z. Zhao, M.-T. Suzuki, R. Arita, Y. Wu, D. Mou, H. Cao, J. Yan, N. Trivedi, and A. Kaminski, Nat. Mater. **15**, 1155 (2016).

[15] K. Deng, G. Wan, P. Deng, K. Zhang, S. Ding, E. Wang, M. Yan, H. Huang, H. Zhang, Z. Xu, J. Denlingher, A. Fedorov, H. Yang, W. Duan, H. Yao, Y. Wu, S. Fan, H. Zhang, X. Chen, and S. Zhou, Nat. Phys. **12**, 1105 (2016).

[16] J. Jiang, Z. K. Liu, Y. Sun, H. F. Yang, C. R. Rajamathi, Y. P. Qi, L. X. Yang, C. Chen, H. Peng, C.-C. Hwang, S. Z. Sun, S.-K. Mo, I. Vobornik, J. Fujii, S. S. P. Parkin, C. Felser, B. H. Yan, and Y. L. Chen, Nat. Commun. **8**, 13973 (2017).

[17] E. Haubold, K. Koepernik, D. Efremov, S. Khim, A. Fedorov, Y. Kushnirenko, J. van den Brink, S. Wurmehl, B. Buchner, T. K. Kim, M. Hoesch, K. Sumida, K. Taguchi, T. Yoshikawa, A. Kimura, T. Okuda, and S. V. Borisenko, Phys. Rev. B **95**, 241108(R) (2017).
[18] S.-Y. Xu, N. Alidoust, G. Chang, H. Lu, B. Singh, I. Belopolski, D. S. Sanchez, X. Zhang, G. Bian, H. Zheng, M.-A. Husanu, Y. Bian, S.-M. Huang, C.-H. Hsu, T.-R. Chang, H.-T. Jeng, A. Bansil, T. Neupert, V. N. Strocov, H. Lin, S. Jia, and M. Z. Hassan, Sci. Adv. **3**, e1603266 (2017).
[19] P. Li, W. Wu, Y. Wen, C. Zhang, J. Zhang, S. Zhang, Z. Yu, S. A. Yang, A. Manchon, and X. Zhang, Nat. Commun. **9**, 3990 (2018).
[20] M. D. Bachmann, N. Nair, F. Flicker, R. Ilan, T. Meng, N. J. Ghimire, E. D. Bauer, F. Ronning, J. G. Analytis, and P. J. W. Moll, Sci. Adv. **3**, e1602983 (2017).
[21] C. Huang, A. Narayan, E. Zhang, Y. Liu, X. Yan, J. Wang, C. Zhang, W. Wang, T. Zhou, C. Yi, S. Liu, J. Ling, H. Zhang, R. Liu, R. Sankar, F. Chou, Y. Wang, Y. Wang, Y. Shi, K. T. Law, S. Sanvito, P. Zhou, Z. Han, and F. Xiu, ACS Nano **12**, 7185 (2018).
[22] Y. Kim, M. J. Park, and M. J. Gilbert, Phys. Rev. B **93**, 214511 (2016).
[23] U. Khanna, S. Rao, and A. Kundu, Phys. Rev. B **95**, 201115(R) (2017).
[24] D. K. Mukherjee, S. Rao, and A. Kundu, Phys. Rev. B **96**, 161408(R) (2017).
[25] K. A. Madsen, E. J. Bergholtz, and P. W. Brouwer, Phys. Rev. B **95**, 064511 (2017).
[26] S.-B. Zhang, F. Dolcini, D. Breunig, and B. Trauzettel, Phys. Rev. B **97**, 041116(R) (2018).
[27] Z. Hou and Q.-F. Sun, Phys. Rev. B **96**, 155305 (2017).
[28] X.-S. Li, S.-F. Zhang, X.-R. Sun, and W.-J. Gong, New J. Phys. **20**, 103005 (2018).
[29] J. Fang, W. Duan, J. Liu, C. Zhang, and Z. Ma, Phys. Rev. B **97**, 165301 (2018).
[30] W. Duan, J. Liu, J. Fang, C. Zhang, and Z. Ma, Phys. Rev. B **98**, 155317 (2018).
[31] S. Uddin, W. Duan, J. Wang, Z. Ma, and J.-F. Liu, Phys. Rev. B **99**, 045426 (2019).
[32] U. Khanna, A. Kundu, S. Pradhan, and S. Rao, Phys. Rev. B **90**, 195430 (2014).
[33] A. F. Andreev, Zh. Eksp. Teor. Fiz. **46**, 1823 (1964) [Sov. Phys. JETP **19**, 1228 (1964)].
[34] G. E. Blonder, M. Tinkham, and T. M. Klapwijk, Phys. Rev. B **25**, 4515 (1982).
[35] J.-X. Zhu, B. Friedman, and C. S. Ting, Phys. Rev. B **59**, 9558 (1999).
[36] J. Cayssol, Phys. Rev. Lett. **100**, 147001 (2008).
[37] C. Benjamin and J. K. Pachos, Phys. Rev. B **78**, 235403 (2008).
[38] J. Linder, M. Zareyan, and A. Sudbø, Phys. Rev. B **80**, 014513 (2009).
[39] W. Chen, R. Shen, L. Sheng, B. G. Wang, and D. Y. Xing, Phys. Rev. B **84**, 115420 (2011).
[40] J. Linder and T. Yokoyama, Phys. Rev. B **89**, 020504(R) (2014).
[41] C. Bai, Y. Zou, W.-K. Lou, and K. Chang, Phys. Rev. B **90**, 195445 (2014).
[42] Y. S. Ang, L. K. Ang, C. Zhang, and Z. Ma, Phys. Rev. B **93**, 041422(R) (2016).
[43] H. Li, Phys. Rev. B **94**, 075428 (2016).
[44] C. W. J. Beenakker, Phys. Rev. Lett. **97**, 067007 (2006).
[45] I. A. Sadovskyy, G. B. Lesovik, and V. M. Vinokur, New J. Phys. **17**, 103016 (2015).
[46] G. C. Paul, P. Dutta, and A. Saha, J. Phys.: Condens. Matter **29**, 015301 (2017).